Tungsten (W) Fractionation in Enstatite Chondrites

Hannah Nechin[1]

Advisors: Dr. Richard Ash[1], Dr. Philip Piccoli[1]

GEOL 394

April 23rd, 2024

Affiliations: [1]University of Maryland College Park

Abstract

This study addresses the discrepancy between expected and observed quantities of siderophilic tungsten (W) in high-iron EH (**E**nstatite-**H**igh) and low-iron EL (**E**nstatite-**L**ow) enstatite chondrites. While it has been assumed that high-Fe EH chondrites contain more metal and W compared to low-Fe EL chondrites, precise bulk Hf/W concentrations show near parity between EH and EL chondrites. This study quantifies the metal content in EH and EL chondrites using image processing and determines W concentrations in the metal phase using laser ablation inductively coupled plasma mass spectrometry (LA-ICP-MS). Image analyses reveal no systematic differences in metal content between EH and EL chondrites, consistent with prior studies. LA-ICP-MS data show uniform W concentrations in both enstatite chondrite groups. The argument against physical metal-silicate separation (Hf-W fractionation) between EH and EL chondrites is thus supported by the findings in this study. These results underscore enstatite chondrites as reliable proxies for understanding the compositions of meteorite parent bodies formed in the inner regions of the protoplanetary disk.

Plain Text Abstract

Meteorites are fragments of extraterrestrial bodies that have made their way to Earth. Chondrites are a type of meteorite made up of sediment from the solar nebula, and they provide a record of the physical and chemical processes of the solar system's formation. Enstatite chondrites, a type of chondrite, are divided into two groups, EH and EL, based on their physical and chemical characteristics. Recent studies have shown that despite EH and EL chondrites being different chemically, they have the same amount of the element tungsten (W). Exploring this discrepancy by looking at the metal content in these meteorites, this study found that the metal and tungsten levels are the same in EH and EL chondrites, which goes against what was previously assumed. The results imply that when the EH and EL parent bodies formed, the metals and other materials had not yet separated from one another, providing greater insight into how planets and asteroids formed during the earliest days of the solar system.

Introduction

Earth is a dynamic body. As a result, the earliest of Earth's history has been lost to over 4.5 billion years of geologic processing. The absence of any record of these early chapters preserved in terrestrial rock compels exploration of the extraterrestrial, namely asteroids and other less-processed bodies in the solar system. Such bodies are significant sources of scientific information because they are considered remnant planetesimals that accreted during the first ~10 million years of solar system development and have remained essentially unchanged since their formation. Meteorites, as Earth-bound samples of such bodies, can thus be considered to more closely resemble the primitive materials from which the solar system formed than any other known object. As such, they can provide important insights into processes related to the accretion and differentiation of planetesimals and planetary bodies.

1.1 Chondrites

Meteorites can be broadly divided into two groups: differentiated and undifferentiated. Differentiated meteorites are formed by the partial or complete melting and differentiation of their parent bodies. Considering that planetary differentiation involves material separation and compositional layering, the compositions of differentiated meteorites are not representative of their bulk parent bodies or the precursory material from which they accreted. The processing experienced by differentiated meteorites results in the obfuscation and overprinting of evidence related to their primordial solar nebular origins.

Unlike differentiated meteorites, undifferentiated meteorites, known as chondrites, are fragments of primitive planetesimals that did not experience melting and igneous differentiation. As unaltered aggregates of sediment from the solar nebula, chondrites allow for the study of the material from the protoplanetary disk.
Although chondritic parent bodies didn't experience melting and differentiation during formation, most experienced subsequent alteration by processes such as aqueous or hydrothermal alteration and thermal or shock metamorphism (Krot et al., 2014; White, 2020). This processing, however, was largely isochemical; the records of the solar nebula's physical and chemical processes are retained. Examining the compositional, textural, and mineralogical characteristics of chondrites can thus provide valuable insight into the conditions and processes that led to the formation and evolution of the solar system.

Chondrites derive their name from chondrules, mm-scale spherical melt droplet particles rich in the silicate minerals olivine and pyroxene. Additional chondritic constituents include refractory inclusions – Ca-Al inclusions (CAIs) and amoeboid olivine aggregates (AOAs) – and Fe-Ni metal, all of which are situated in a fine-grained matrix (Krot et al., 2014; White, 2020). Textural, compositional, and mineralogical features of these constituents indicate that they formed while dispersed in the solar nebula and were subsequently aggregated to form the chondritic parent bodies (White, 2020). However, not all chondrites possess all of these components; chondrites encompass a wide range of mineralogical, chemical, and textural characteristics, likely indicative of heterogeneities within the solar nebula.

1.2 Enstatite Chondrites

Amongst the major chondrite classes, enstatite chondrites stand out as the most reduced natural assemblages known from the solar system. The highly reduced, anhydrous nature of these meteorites, coupled with oxygen isotope ratios indistinguishable from those of the Earth and Moon, suggests that enstatite chondrites formed in the inner solar system and possess a potential genetic link to the material from which Earth accreted (Kallemeyn & Wasson, 1986; Weisberg & Kimura, 2012). The extremely low oxygen fugacity (fO_2) conditions in which enstatite chondrites formed are mirrored by their characteristic mineralogy. As illustrated in the Urey-Craig diagram [Figure 1], the Fe in enstatite chondrites is located almost entirely in the metal and sulfide phases. Consequently, the silicate minerals found in enstatite chondrites are free of FeO, leading to the ubiquity of their namesake, pure Mg-endmember enstatite ($MgSiO_3$). Additional distinguishing features of enstatite chondrites include Si-bearing Fe-Ni metal and sulfides of typically lithophile elements (e.g., oldhamite (CaS), niningerite (MgS)), indicating formation under highly reducing conditions (Mason, 1966; Keil, 1968).

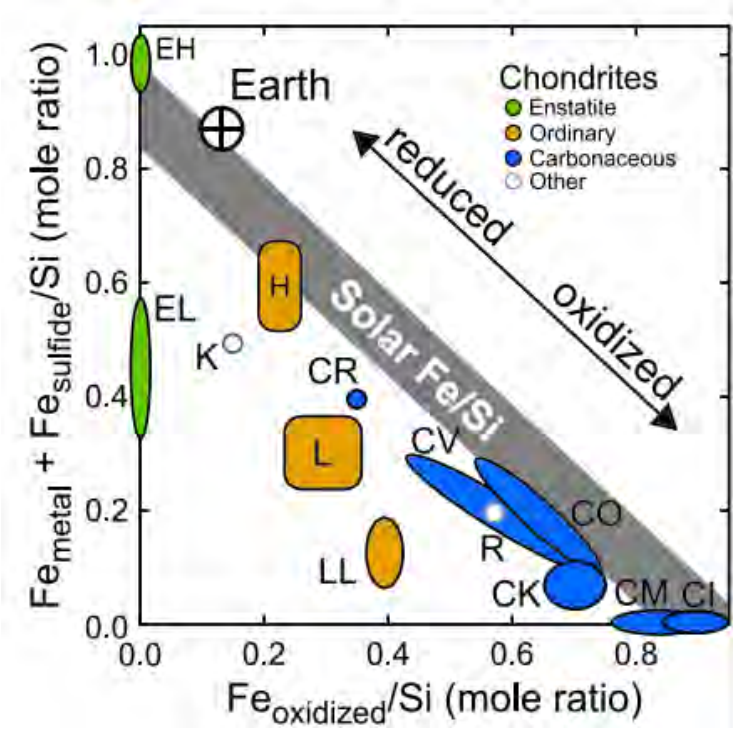

Figure 1: From Yoshizaki et al. (2021). A Urey-Craig diagram illustrates chondrite groups' relative iron contents and oxidation states. Chondrite groups document a diverse range of oxidation states likely established through a mix of nebular and asteroidal processes. These levels of oxidation are indicated by the distribution of iron among its three standard oxidation states: 0 (found in Fe-Ni metal and Fe sulfides), +2 (found in silicates), and +3 (found in oxides). The Urey-Craig diagram (after Urey and Craig, 1953) visually depicts the range of oxidation states recorded in the carbonaceous, ordinary, and enstatite chondrite groups (Krot et al. 2014).

As proposed by Sears et al. (1982), the accepted classification of enstatite chondrites is subdivided into two groups based on mineralogy and bulk chemistry: high-Fe EH chondrites and low-Fe EL chondrites. Further diagnostic criteria of EH chondrites include higher abundances of opaque minerals and the presence of niningerite ((Mg, Fe)S), in addition to enrichments of Si in kamacite (α-Fe, Ni), and the presence of perryite $((Ni, Fe)_x(Si, P)_y)$. In contrast, EL chondrites are characterized by the presence of alabandite ((Mn, Fe)S) (Lin & El Goresy, 2002; Barrat et al., 2023).

Figure 2: Cross section of a piece of the highly brecciated EH chondrite, Abee (EH4). High metal abundances, as illustrated by the large quantity of light-grey specks, represent the significantly reduced conditions in which these chondrites formed.

Whereas bulk chemistry shows clear distinctions between EH and EL chondrites based on Fe content, uncertainty arises when considering data from Keil (1968). As the only petrographic study done to determine modal abundances in equilibrated enstatite chondrites, which was conducted using point-counting analyses over 50 years ago, quantities of Fe metal show no such clear distinctions, with iron-rich EH chondrites showing 29 to 35% Fe and iron-poor EL chondrites showing 20 to 29% Fe (Javoy et al., 2010).

1.3 Hf-W Geochronometer

With a half-life of 8.9 ± 0.1 Ma, the decay of short-lived ^{182}Hf to stable ^{182}W serves as the basis for a decay scheme well-suited for studying events within the first ~60 Ma of solar system history. Considering that planetary bodies formed within the first ~100 Ma, the time interval associated with the decay of extinct ^{182}Hf is well-suited for studying planetary accretion, differentiation, and evolution (Kleine, 2009). Making this chronometer particularly valuable are the distinct chemical properties of Hf and W. While Hf is a lithophile (Si-loving) element, W is a moderately siderophile (Fe-loving) element. As ^{182}Hf decayed to ^{182}W, siderophilic W preferentially partitioned into the metal phase while the silicate portion retained lithophilic Hf (Kleine & Walker, 2017). Such strong partitioning during metal-silicate segregation forms the basis for numerous significant geochronologic applications, such as determining model ages of core formation, and the dating of chondrites and the thermal histories of their parent bodies (Kleine et al., 2008).

2. Objectives of Research

Given the highly reduced nature of enstatite chondrites, it has been largely assumed that the majority of Fe exists in its metallic state. The high-Fe EH chondrites are thus expected to contain greater quantities of metal and, in direct consequence, siderophilic W. Conversely, low-Fe EL chondrites are assumed to contain less metal and correspondingly lower amounts of W. However, based on Hf/W concentrations collected by Dr. Jan Hellmann via bulk sample dissolution and isotope dilution, coupled with data from Lee & Halliday (2000), W concentrations are nearly identical in both EH and EL chondrites [Fig. 3]. This results in a discrepancy between expected and observed W quantities.

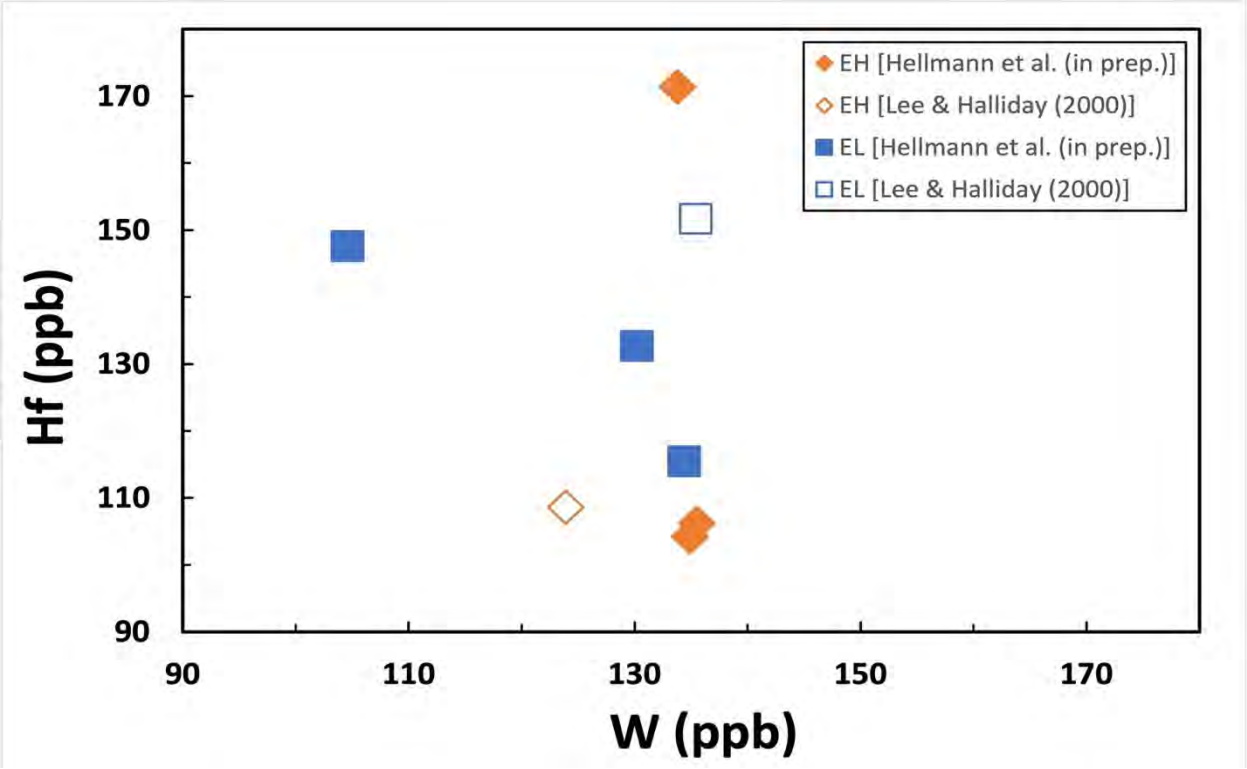

Figure 3: Plot of W vs. Hf concentrations (in ppb). Modified from Jan Hellmann (Personal Communication, 2023)

This project was conducted in two stages to address the potential causes of this discrepancy. The first stage used image analysis to quantify metal content in EH and EL chondrites. Stage 1 consists of the following hypotheses:

> **Null Hypothesis 1: There is no difference in the amount of Fe-metal between EH and EL chondrites.**
>
> **Alternative Hypothesis 1: EH chondrites have more metal than EL chondrites.**

The second stage involves determining W concentrations in metal grains using laser ablation inductively coupled plasma mass spectrometry (LA-ICP-MS). For this stage, the hypotheses are as follows:

> **Null Hypothesis 2: There is no difference in the average W concentrations of metal grains between EH and EL chondrites.**
>
> **Alternative Hypothesis 2: The average W content of the metal grains is lower in EH chondrites than in EL chondrites.**

In exploring W fractionation in enstatite chondrites, this study aims to provide additional insight into how this element behaves in highly reduced conditions in order to facilitate increasingly successful applications of the Hf-W chronometer.

3. Methods

Fragments of 8 enstatite chondrites were provided by the American Museum of Natural History and the Smithsonian Institution National Museum of Natural History. Six of the samples are mounted in epoxy plugs in the form of thick sections, and the remaining two samples are thin sections. Of these samples, 4 are classified as EH chondrites, and 4 are classified as EL chondrites.

Table 1: List of meteorite samples to be considered as part of this study. Meteorite types are based on the online Meteoritical Bulletin Database (www.lpi.usra.edu/meteor/). Abbreviations: AMNH – American Museum of Natural History. SI – Smithsonian Institution

Name	Type	Sample Source
Daniel's Kuil	EL6	AMNH
Jaih deh Kot Lalu	EL6	AMNH
Khairpur	EL6	AMNH
Pillistfer	EL6	AMNH
Abee	EH4	SI
Indarch	EH4	SI
St. Mark's	EH5	SI
Saint Sauveur	EH5	SI

To ensure maximum clarity during image analysis and minimize pre-existing scratches on metal grains, the samples were given an additional polish using a combination of fine-grit abrasive paper and 1.0-micron aluminum-oxide powder.

3.1 Image Processing

3.1.1 Image Acquisition and Mosaic Assembly

A Nikon Eclipse LV100 Polarizing microscope with a QImaging Micropublisher 5.0-RTV camera was used to take photomicrographs of the polished samples using reflected light microscopy. Each photomicrograph was taken using the 5x-magnification objective lens. The photomicrographs were optimized to produce maximum contrast between the silicate, sulfide, and metal phases. Two series of images were taken for each sample: one for mosaic assembly and one for image analysis. The series of images taken for mosaic assembly contained overlap.
The images taken for the purpose of image analysis were taken in such a way as to exclude background and overlap.

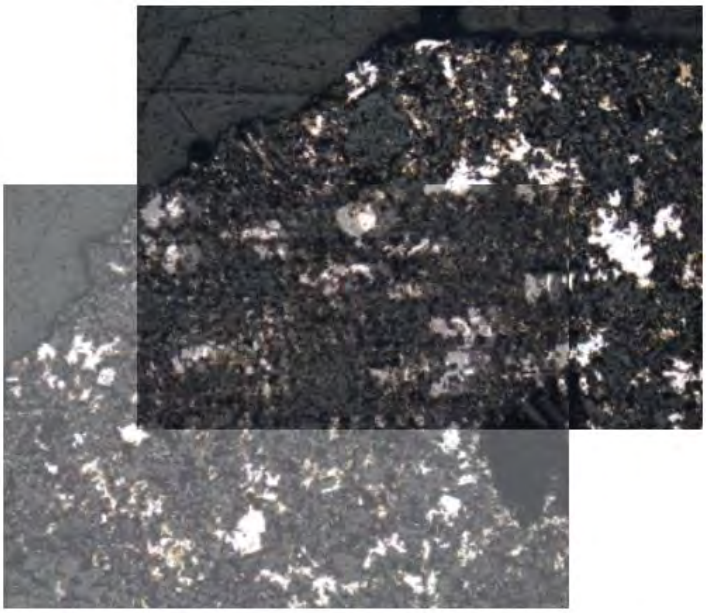

Figure 1: Two reflected light photomicrographs with overlapping sections. The bottom photomicrograph was lowered in opacity and placed on top of the other to accurately align the overlapping section. Based on blurriness, the photomicrographs are not in alignment.

Following image acquisition, the overlapping photos were imported into Adobe Illustrator to stitch them together to create a composite sample mosaic. Taking two images with overlapping sections, one was lowered in opacity and placed on top of the other. When not in alignment, the area in which the images overlapped was blurry. When in alignment, the overlapping area came fully into focus.

In addition to serving as guides for navigating the sample during EPMA and LA-ICP-MS analyses, composite sample mosaics provided insight into sample heterogeneity and the abundance and distribution of phases.

3.1.2 Image Segmentation

Using Fiji/ImageJ photo-analytical software, the background- and overlap-free reflected light photomicrographs were analyzed for metal content using image segmentation, specifically the global thresholding-based segmentation method.

Image segmentation is a computer vision technique that assigns labels to groups of pixels to partition an image into segments to inform object detection and extraction. Various methods and algorithms exist for image segmentation, such as region-based and edge-detection segmentation. For this study, the global threshold-based image segmentation method was utilized. Global thresholding is an image segmentation technique that converts a grayscale image, where pixel intensities range from 0 to 255, into a binary mask by classifying each pixel as either black or white based on its intensity value relative to a set threshold value. For example, in setting a threshold of 100, pixels below or equal in intensity to 100 will be assigned a value of 0 (black), and pixels with intensity values greater than 100 will be assigned a value of 1 (white).

3.1.2.1 Global Threshold-Based Image Segmentation and Data Collection

Upon opening the TIFF photomicrograph file in Fiji, images underwent grayscale (8-bit) conversion (Image > Type > 8-bit). To isolate the targeted phase for analysis, the threshold of the 8-bit image was adjusted until the highlighted sections of the photomicrograph corresponded to the metal grains (Image > Adjust > Threshold). The optimal threshold value was ascertained based on empirical observation by comparison with the original color photomicrograph. Once the threshold value was determined, said threshold was applied to the grayscale image, generating a binary mask. Pixels with intensities above the threshold were classified as metal (foreground), while pixels below the threshold were classified as background. This resulting binary image was then analyzed using Fiji's "Measure" function, generating a percent area value representing the metal phase relative to the total image area (Analyze > Measure).

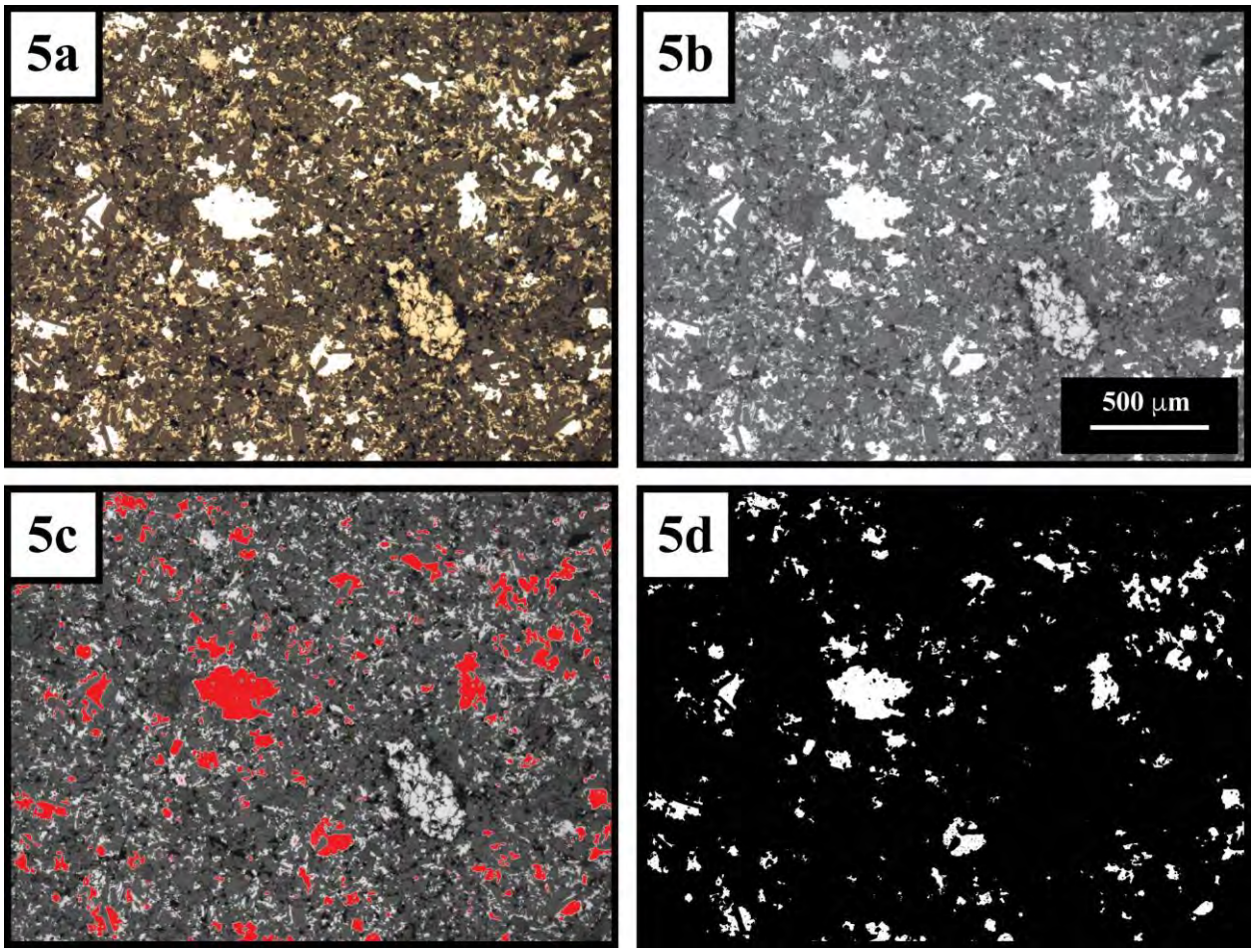

Figure 5: Image Segmentation Steps Illustrated Using Abee (EH4) Photomicrograph 5a) Original color photomicrograph **5b)** Photomicrograph converted to grayscale (8-bit) **5c)** Threshold determination. Areas highlighted in red are those with pixel intensity values that are greater than the assigned threshold value. **5d)** Binary image generated from the application of the threshold.

3.2 EPMA

Electron microprobe data was collected at the Advanced Imaging and Microscopy (AIM) Lab at the University of Maryland. The JEOL JXA-8900 Electron Probe Microanalyzer was used for qualitative mineral identification via energy dispersive spectroscopy (EDS). Operating conditions include a sample current of 20 nA, an accelerating voltage of 15kV, and electron beams ranging in size from 1 to 50 μm. EPMA analyses were conducted on one EH sample, St. Mark's (EH5) and one EL sample, Pillistfer (EL6).

3.3 LA-ICP-MS

Laser ablation inductively coupled plasma mass spectrometry (LA-ICP-MS) measurements were performed over the course of two visits to the Carnegie Institution for Science in Washington, D.C., using an ICapQ ICP-MS coupled to an Iridia laser ablation system with an output wavelength of 193 nm.

For the first batch of analyses, the isotopes ^{29}Si, ^{31}P, ^{57}Fe, ^{59}Co, ^{61}Ni, ^{63}Cu, ^{71}Ga, ^{73}Ge, ^{99}Ru, ^{101}Ru, ^{103}Rh, ^{105}Pd, ^{108}Pd, ^{182}W, ^{183}W, ^{185}Re, ^{189}Os, ^{193}Ir, ^{195}Pt, ^{197}Au, were used for

quantification of concentration. Samples were ablated using 50 μm spot sizes with a repetition rate of 20 Hz, and fluence energy ranged from 2.5-3.5 J cm^{-2}. Twenty seconds of background and approximately 1 minute of sample material were collected from ablation. During the first visit, the samples Pillistfer (EL6), St. Mark's (EH5), and Khairpur (EL6) were measured.
For the second batch of analyses, ^{95}Mo and ^{97}Mo were measured in addition to all of the isotopes listed above. The only change between the first and second batch of analyses was doubling the counting time for the W isotopes. The remaining five samples were measured during the second visit.
Dr. Richard Ash processed the data manually in Excel using the standard reference iron meteorites Hoba and Coahuila. For each analysis, the Fe + Ni + Co abundances were forced to sum to 100%.

Annotations were made on sample image mosaics with each laser ablation analysis, documenting the identity of the metal grain being ablated and the label associated with the analysis. This documentation facilitated subsequent grain size measurements. However, such annotations were limited to the St. Mark's (EH5), Pillistfer (EL6), Indarch (EH4), Daniel's Kuil (EL6), and Jaih deh Kot Lalu (EL6) samples. Due to not being in possession of their sample image mosaics at the time of laser ablation analyses, annotations could not be made for the Khairpur (EL6), Abee (EH4), and Saint Sauveur (EH5) samples.

3.4 Grain Size Measurements

Fiji/ImageJ photo-analytical software was used to perform grain-size measurements on the metal grains analyzed via LA-ICP-MS. These measurements were conducted to facilitate comparison with studies that employed wet chemistry methodologies to measure concentrations in coarse- and finer-grained metal separates (Hellmann et al. 2024).

After opening the TIFF photomicrograph file in Fiji, the scale of the image was established using the "Set Scale" tool, which allows for the calibration of pixel dimensions to physical units. Given that all the photomicrographs were captured using the 5x magnification objective lens, the width of the image was calibrated to 2.7 mm. After setting the scale, the line tool was utilized to draw a line along the long axis of the selected metal grain. Employing the "Measure" function, the software then calculated the length of the line based on the established scale.

4. Results

4.1 Image Processing

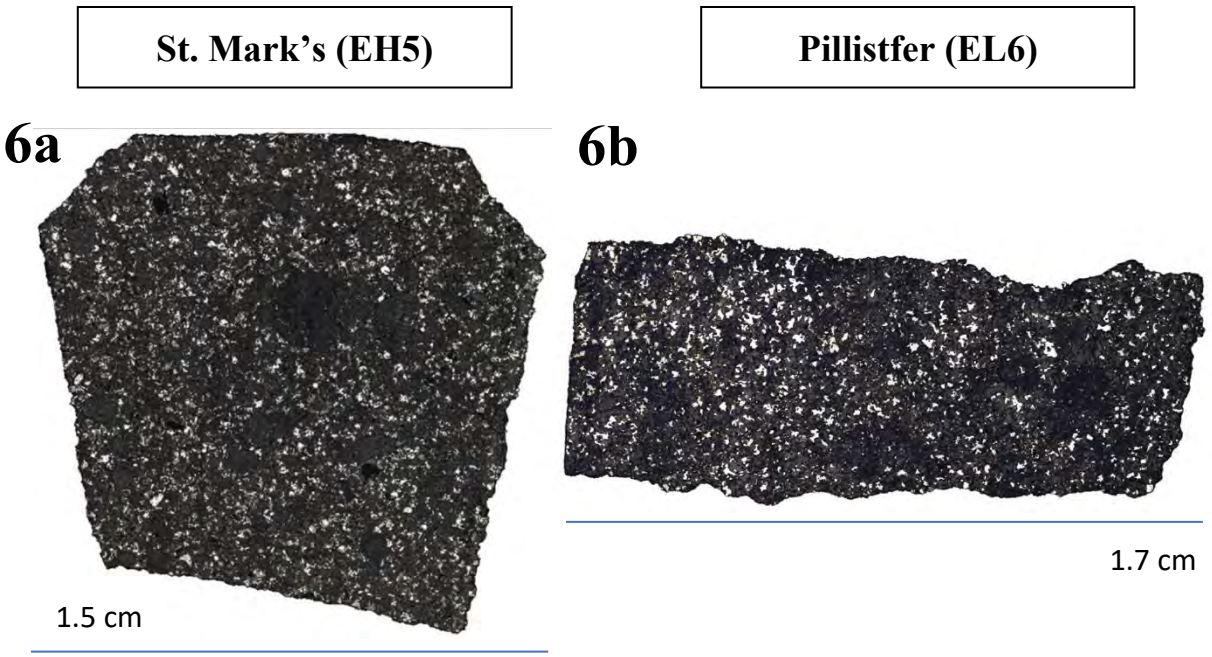

Figure 6: Examples of composite photomicrograph mosaics **6a)** Composite photomicrograph mosaic of St. Mark's (EH5); composed of reflected-light photomicrographs taken at 5x magnification. **6b)** Composite photomicrograph mosaic of Pillistfer (EL6); composed of reflected-light photomicrographs taken at 5x magnification.

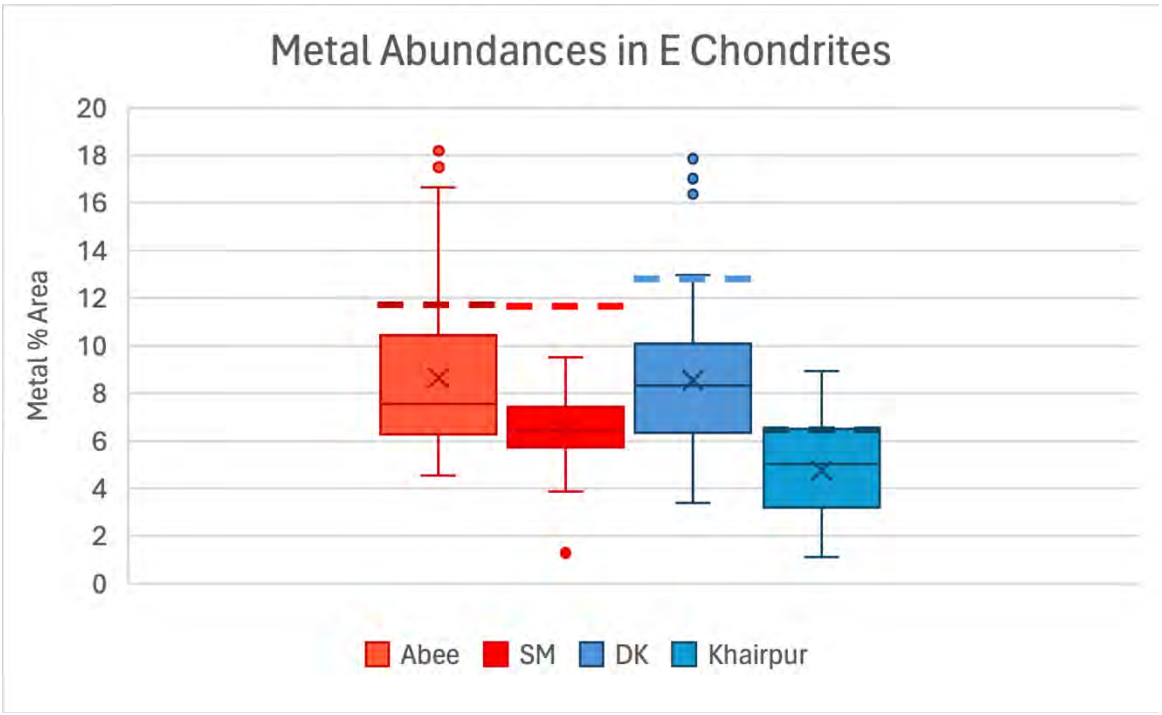

Figure 7: A box and whisker plot illustrating the distribution of metal % area measurements obtained through image processing for EH chondrites Abee (EH4) and St. Mark's (EH5)) and EL chondrites Daniel's Kuil (EL6) and Khairpur (EL6). The dashed lines denote the metal modal abundance value for a given meteorite as determined from the Keil (1968) point counting analyses. Values from Keil (1968) were converted from wt. % to area %.. The Abee (EH4) data set consists of 29 data points, the St. Mark's (EH5) data set consists of 37 data points, the Daniel's Kuil (EL6) data set consists of 22 data points, and the Khairpur (EL6) data set consists of 18 data points.

4.2 EPMA EDS

Table 2 and 3 list the minerals identified for St. Mark's (EH5) and Pillistfer (EL6), respectively, as determined through analyses of EDS spectra.

Table 2: Minerals identified through analysis of EDS spectra for the St. Mark's (EH5) sample.

St. Mark's (EH5)

Mineral Name	Mineral Formula
Enstatite	$MgSiO_3$
Kamacite	α-(Fe,Ni)
Perryite	$(Ni,Fe)_x(Si,P)_y$
Niningerite	[(Mg,Fe)S]
Troilite	FeS
Daubreelite	$FeCr_2S_4$
Oldhamite	CaS
Quartz	SiO_2

Table 3: Minerals identified through analysis of EDS spectra for the Pillistfer (EL6) sample.

Pillistfer (EL6)

Mineral Name	Mineral Formula
Enstatite	$MgSiO_3$
Kamacite	α-(Fe,Ni)
Troilite	FeS
Daubreelite	$FeCr_2S_4$
Alabandite	(Mn,Fe)S
Schreibersite	$(Fe,Ni)_3P$

4.3 LA-ICP-MS

Four EH and four EL chondrites underwent laser ablation analyses. Six to eight metal grains were ablated per sample.

Figure 8: CI-chondrite normalized (Lodders & Fegley, 1998) elemental abundance patterns of individual EH chondrite samples obtained via LA-ICP-MS analyses. Each line corresponds to an analysis of a single metal grain. For St. Mark's (EH5) and Indarch (EH4), analyses conducted on coarse metal grains (>250 μm) are depicted in shades of blue, while analyses on finer-grained metal (60-250 μm).are depicted in shades of yellow.

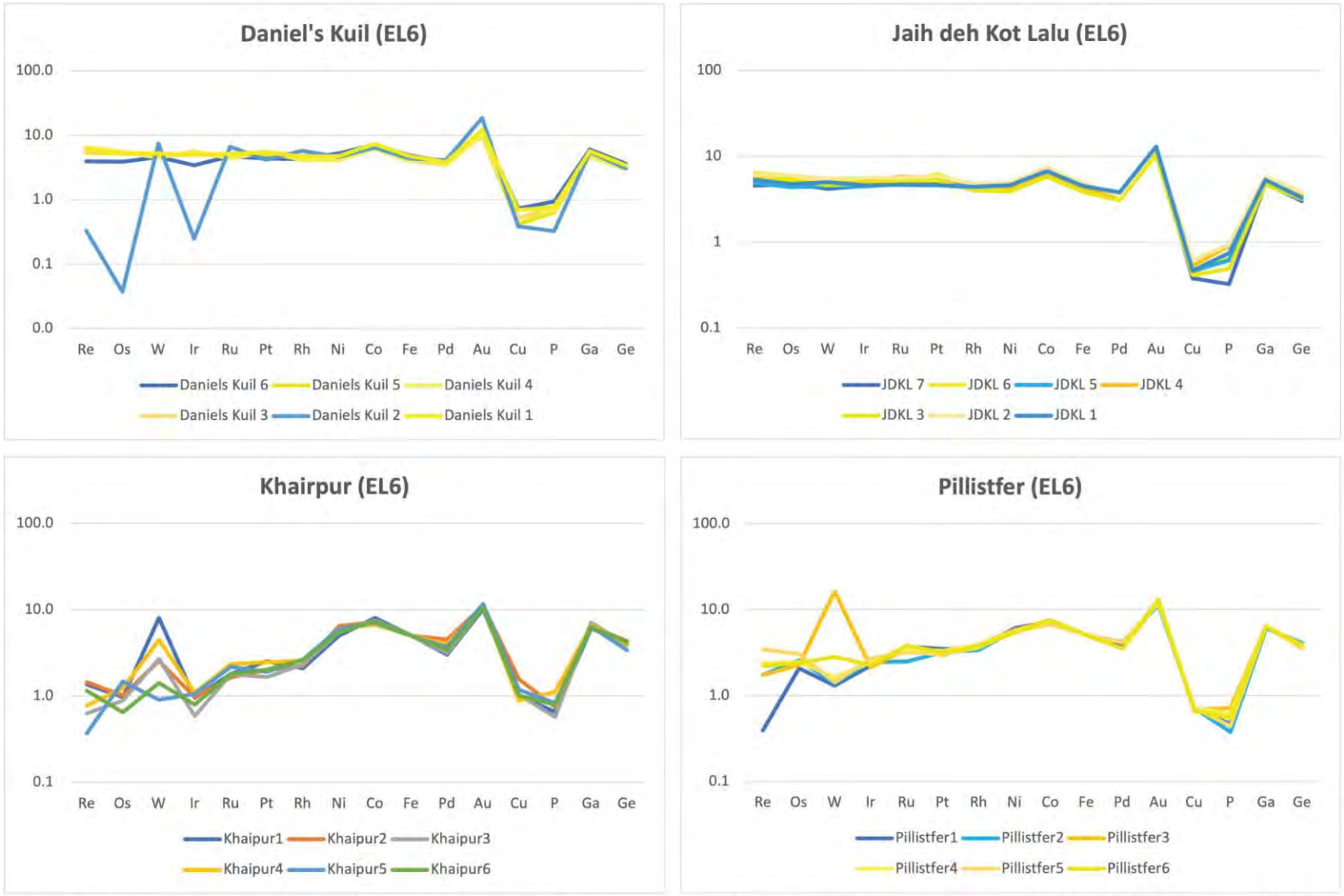

Figure 9: CI-chondrite normalized (Lodders & Fegley, 1998) elemental abundance patterns of individual EL chondrite samples obtained via LA-ICP-MS analyses. Each line corresponds to an analysis of a single metal grain. For Daniel's Kuil (EL6), Pillistfer (EL6), and Jaih deh Kot Lalu, analyses conducted on coarse metal grains (>250 μm) are depicted in shades of blue, while analyses on finer-grained metal (60-250 μm).are depicted in shades of yellow.

Table 4: Average elemental concentrations obtained via LA-ICP-MS analyses. Concentrations reported in ppm.

Sample	Re	1σ	Os	1σ	W	1σ	Ir	1σ	Ru	1σ	Pt	1σ	Rh	1σ	Ni	1σ
Abee (EH4)	0.18	± 0.09	1.75	± 0.8	0.4	± 0.2	1.8	± 0.8	3.2	± 1.0	4.3	± 1.4	0.7	± 0.26	71682	± 4214
Indarch (EH4)	0.12	± 0.06	1.4	± 0.8	0.42	± 0.08	1.3	± 0.8	2.8	± 0.9	3.3	± 1.4	0.52	± 0.11	56663	± 11099
St. Sauveur (EH5)	0.19	± 0.06	1.9	± 0.3	0.44	± 0.11	1.8	± 0.3	3.2	± 0.5	4.0	± 0.8	0.58	± 0.09	77492	± 13850
St. Mark' s (EH5)	0.16	± 0.03	1.9	± 0.08	0.46	± 0.13	1.8	± 0.15	2.9	± 0.3	3.5	± 0.4	0.49	± 0.06	49750	± 7826
Pillistfer (EL6)	0.09	± 0.04	1.3	± 0.2	0.52	± 0.71	1.3	± 0.1	2.7	± 0.6	3.4	± 0.2	0.59	± 0.04	61907	± 2561
Khairpur (EL6)	0.04	± 0.02	0.53	± 0.15	0.45	± 0.40	0.51	± 0.11	1.7	± 0.4	2.3	± 0.4	0.39	± 0.04	62387	± 5613
Jaih deh Kot Lalu (EL6)	0.20	± 0.02	2.5	± 0.3	0.49	± 0.05	2.3	± 0.2	3.5	± 0.3	5.0	± 0.5	0.59	± 0.04	48818	± 3771
Daniel' s Kuil (EL6)	0.17	± 0.08	2.0	± 1.0	0.54	± 0.11	1.9	± 1.0	3.4	± 0.5	4.7	± 0.6	0.62	± 0.08	50180	± 4545

Sample	Co	1σ	Fe	1σ	Pd	1σ	Au	1σ	Cu	1σ	P	1σ	Ga	1σ	Ge	1σ	Mo	1σ
Abee	3333	± 159	924986	± 4250	2.9	± 0.4	2.0	± 0.1	506	± 112	3582	± 794	73	± 10	180	± 19	----	
Indarch	3178	± 563	797362	± 194155	2.2	± 0.5	1.8	± 0.4	209	± 211	1219	± 1113	49	± 10	171	± 40	2.3	± 0.7
St. Sauveur	3776	± 672	970468	±. 179583	2.5	± 0.4	2.4	± 0.5	498	± 71	2530	± 507	77	± 13	167	± 28	3.2	± 0.6
St. Mark' s	2822	± 512	711518	± 118628	2.1	± 0.3	1.4	± 0.3	137	± 64	185	± 56	49	± 9	117	± 15	1.3	± 0.20
Pillistfer	3690	± 159	934404	± 2562	2.7	± 0.2	1.8	± 0.09	90	± 3.2	515	± 122	55	± 1	126	± 6.8	----	
Khairpur	3708	± 222	933905	± 5439	2.4	± 0.3	1.6	± 0.07	145	± 32	768	± 181	57	± 3	133	± 11	----	
Jaih deh Kot Lalu	3300	± 249	801057	± 55626	1.9	± 0.1	1.7	± 0.1	61	± 10	651	± 212	49	± 4	113	± 9	2.4	± 0.3
Daniel' s Kuil	3359	± 260	813200	± 64297	2.1	± 0.1	1.8	± 0.5	70	± 18	672	± 201	50	± 5	108	± 9	2.2	± 0.2

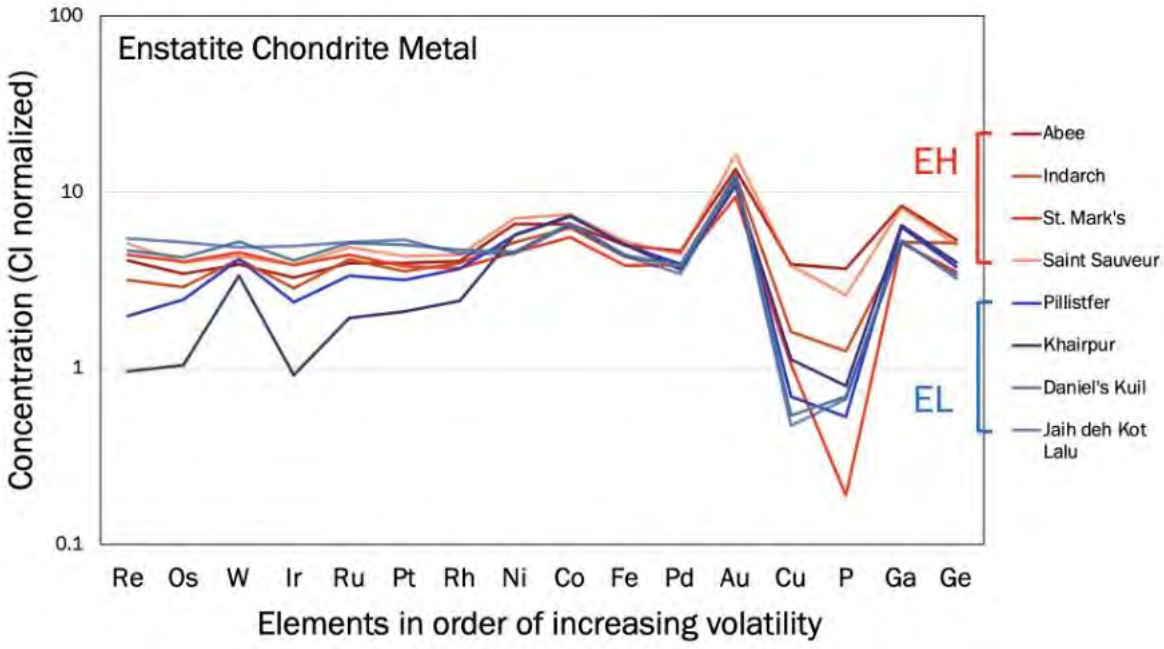

Figure 10: CI-chondrite (Lodders and Fegley, 1998) normalized elemental abundance pattern obtained via LA-ICP-MS analyses. Each colored line corresponds to a meteorite sample. The concentrations illustrated are the averaged values from the 6 to 8 laser ablation analyses conducted on metal grains within each sample.

5. Uncertainty Analysis

5.1 Image Processing

The enstatite chondrite photomicrographs presented challenges for analysis using the global thresholding image segmentation technique, primarily due to overlapping intensity values between metal and sulfide grains. This overlap was likely the result of multiple factors, including areas of rust on certain metal grains, uneven sample surface topography, and an inadequate polish of thick sections. Additionally, variations in lighting further compounded the issue of hue overlap. Uneven lighting resulted in shadows along the photomicrograph edges and areas of highlight toward the image center. Consequently, efforts to segment metal grains became challenging exercises in attempting to find a balance between inevitable degrees of over- and under-segmentation.

Acknowledging the limitations posed by thresholding segmentation, other avenues of image segmentation were explored, namely techniques that combined image processing with machine learning. This manifested as the Trainable Weka Segmentation (TWS) Fiji plugin. Although TWS results were auspicious, this method had a considerable drawback: segmenting a single photomicrograph required significant time and computing power, prompting a return to threshold-based segmentation.

Recognizing the challenges associated with the threshold methodology, further uncertainty lies with determining a threshold value. Optimal threshold values for the enstatite chondrite photomicrographs were determined empirically by visual comparison with the original color photomicrograph. This process of selecting a threshold value is highly subjective and dependent on

individual interpretation; two qualified individuals, each performing segmentation on the same image, are likely to choose different threshold values. Depending on the spread of pixel intensities in a photo, minor variations to the threshold value can lead to significant changes in the segmentation result, potentially causing inaccuracies.

The uncertainty associated with the global thresholding segmentation method, specifically the determination of a threshold value, was evaluated using a combination of two approaches: sensitivity analysis and threshold bracketing. Sensitivity analysis involved varying the threshold over a range of values and assessing the variability in segmentation results, providing insight into the sensitivity of the segmentation outcomes to perturbations in the threshold value [Figure 10]. This was conducted on one photomicrograph from each of the four samples that underwent image processing analyses.

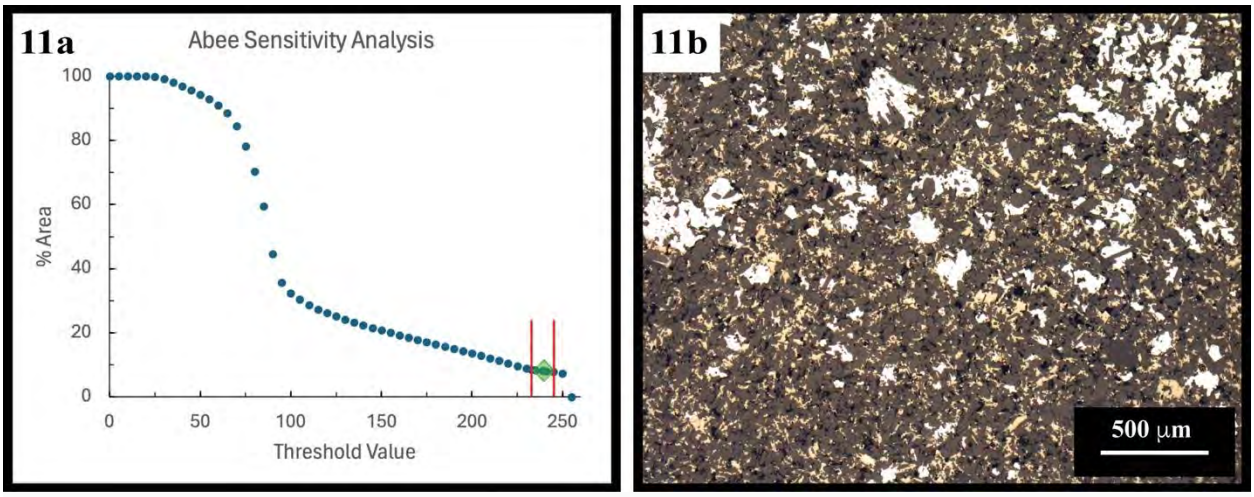

Figure 11: Sensitivity Analysis on Abee (EH4) **11a)** A plot illustrating the different % area measurements that result from perturbing the threshold. The green diamond represents the threshold applied to isolate the metal grains. The red lines are the upper and lower threshold bounds. **11b)** The photomicrograph from Abee used for the sensitivity analysis.

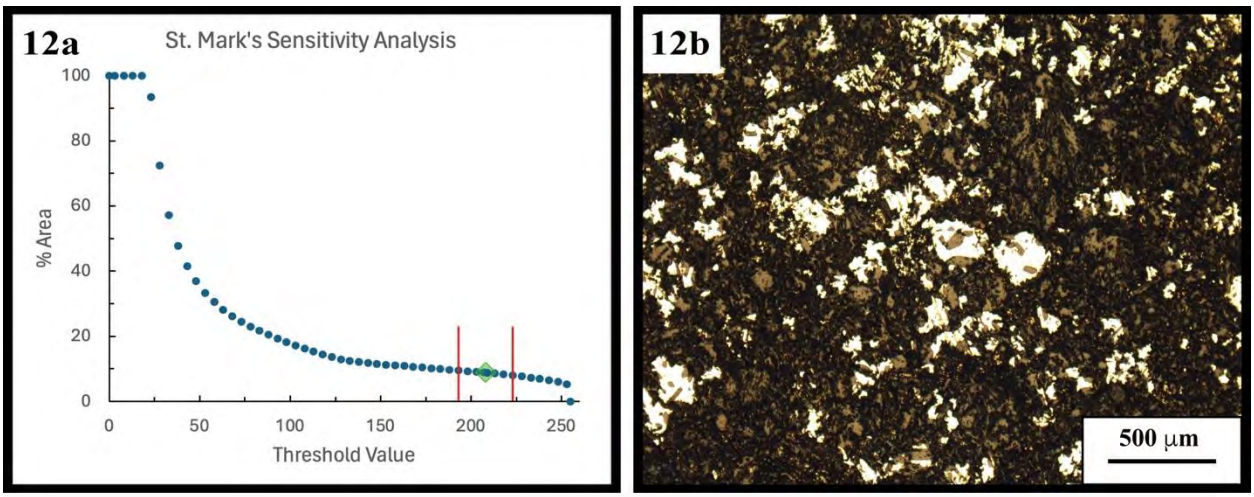

Figure 12: Sensitivity Analysis on St. Mark's (EH5) 12a) A plot illustrating the different % area measurements that result from perturbing the threshold. The green diamond represents the threshold applied to isolate the metal grains. The red lines are the upper and lower threshold bounds. **12b)** The photomicrograph from St. Mark's used for the sensitivity analysis.

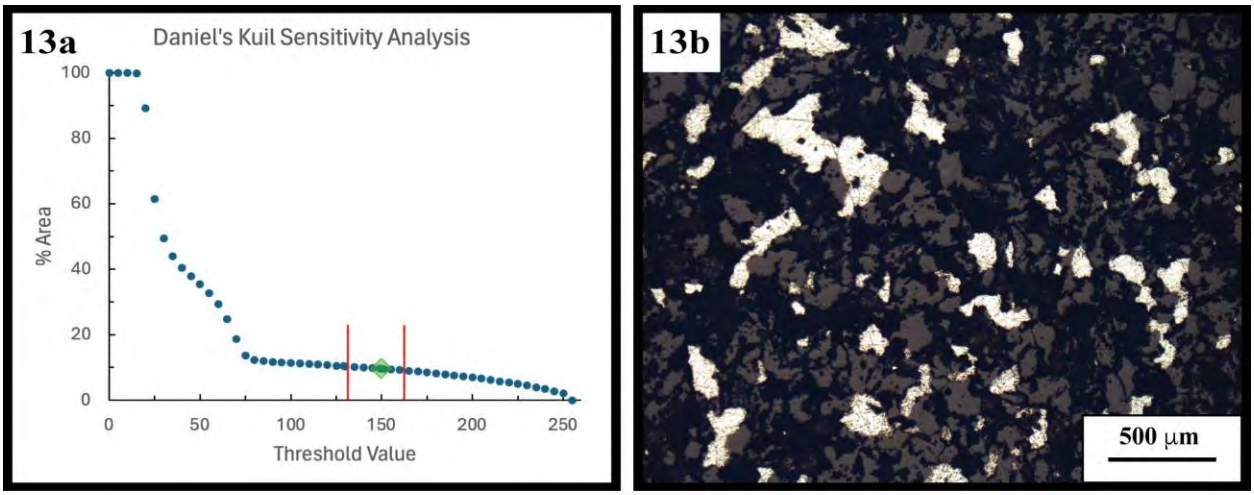

Figure 13: Sensitivity Analysis on Daniel's Kuil (EL6) **13a)** A plot illustrating the different % area measurements that result from perturbing the threshold. The green diamond represents the threshold applied to isolate the metal grains. The red lines are the upper and lower threshold bounds. **13b)** The photomicrograph from Daniel's Kuil used for the sensitivity analysis.

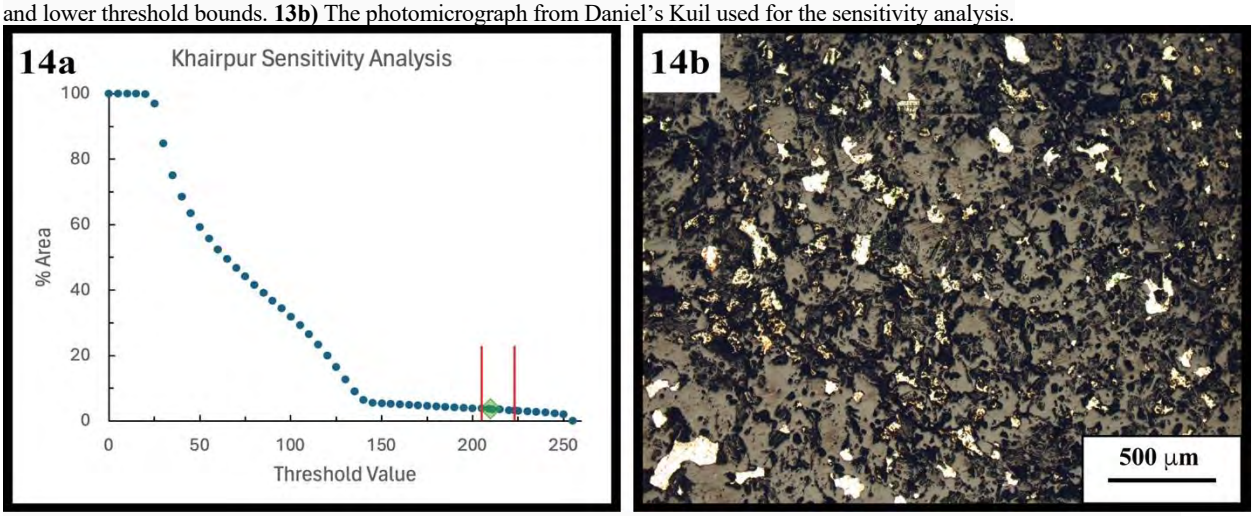

Figure 14: Sensitivity Analysis on Khairpur (EL6) **14a)** A plot illustrating the different % area measurements that result from perturbing the threshold. The green diamond represents the threshold applied to isolate the metal grains. The red lines are the upper and lower threshold bounds. **14b)** The photomicrograph from Khairpur used for the sensitivity analysis.

The sensitivity analyses conducted on the four samples reveal that subtle adjustments to the threshold around the pixel intensities linked to the metal grains have minimal impacts on the % area measurements. In other words, minor variations in the threshold value used to separate the metal grains do not significantly affect the % area measurements.

Threshold bracketing was utilized to establish upper and lower bounds on a given threshold value deemed most representative of the metal phase. An upper bound threshold was determined where it was certain that, for the range of intensity values that made up the metal grains, the threshold excluded metal value intensities, and the entirety of the metal grain was not fully detected at that threshold. i.e., images were purposefully under-segmented. This was repeated for a lower bound, where a threshold was set to include pixel intensities, thereby intentionally over-segmenting the metal grains. Percent area measurements were taken at these upper and lower bounds. Bracketing thus provided a range within which the actual metal threshold and % area values lie.

Lastly, standard deviations were computed to quantify the variability in segmentation outcomes for a given sample, contributing insight into sample heterogeneity [Table 4].

5.2 LA-ICP-MS

The iron meteorites Hoba and Coahuila were used as external standards for calculating tungsten content and assessing measurement accuracy. Using W in Hoba to calculate the W concentration in Coahuila, measurements were reproduced within 11% of the accepted values using Fe as an internal standard.

Internal reproducibility was evaluated by examining the variation between analyses within each sample. Variations in element concentrations within a set of sample analyses were attributed to the inherent variability of natural meteorite samples, potential sample heterogeneities, or systematic errors from the mass spectrometer.

Comparing the concentration values measured using LA-ICP-MS to those reported in the literature served as an additional method of evaluating uncertainty. Such comparisons are included in section 6.2.2 of the discussion.

6. Discussion

6.1 Image Processing

The determination of modal abundance through image processing relies on the assumption that 2-dimensional images can be used to accurately represent the 3-dimensional characteristics of the sample. This assumption treats area measurements as proxies for volume, a sound approach for homogeneous materials. However, such an assumption cannot be applied to heterogeneous materials like enstatite chondrites, as the 2-dimensional representation is unlikely to fully capture the volume distribution. Constrained by the small sample sizes, which prevented evaluation of these meteorites in 3-D, sample homogeneity was assumed, and 2-dimensional images were used as analogs for 3-dimensional characteristics. Consequently, the results presented in this study may not accurately reflect the modal distribution within these samples. It is a recognized limitation of this work.

Due to their nature as loosely cemented aggregates of sediment from the solar nebula, the enstatite chondrite samples posed significant challenges during the polishing process due to their high susceptibility to plucking. The formation of holes from plucked grains potentially influenced the modal abundance results, as the image thresholding process classified these areas as silicate. While this study did not directly assess the impact of these holes on the percent area measurements, it is speculated that their effect was minimal. However, it is recommended that future studies employing image analysis techniques utilize thin sections to mitigate potential inaccuracies arising from holes in the samples.

Differences in sample sizes necessitated varying numbers of photomicrographs to image each sample. As metal % area measurements were taken for each photomicrograph, the dataset sizes for each sample vary. Instead of reducing the size of the datasets to achieve parity for comparative analysis purposes, the decision was made to evaluate the uneven datasets as is. This decision aimed to circumvent potential selection bias, sample misrepresentation, and other inaccuracies likely to result from shrinking datasets.
This being said, there is a notable disparity between dataset sizes, with the EH dataset comprising 66 data points and the EL dataset comprising 40. Such differences may impact the statistical significance of the EH vs. EL comparison and interpretations of sample heterogeneity.

6.1.1 Comparison to Literature

Table 5: Modal abundances of metal measured in enstatite chondrites via image processing compared to point counting analyses from the literature (Keil, 1968). All values are reported as % area, with values from the literature having been converted from wt.% to % area. *n* denotes the size of the dataset.

Sample	Type	*n*	Fe-Ni Metal	Fe-Ni Metal
			This Work	Keil (1968)
Abee	EH4	29	8.74% ± 3.28 (1σ)	11.85 %
St. Mark's	EH5	37	6.45% ± 1.47 (1σ)	11.7%
Daniel's Kuil	EL6	22	8.62% ± 2.82 (1σ)	12.7%
Khairpur	EL6	18	4.62% ± 2.16 (1σ)	6.25%

The metal content percentages reported in this study are consistently lower than the results obtained from the point-counting analyses conducted by Keil (1968). This discrepancy likely arises from errors associated with the global-threshold segmentation method and under-segmentation of metal grains. Nevertheless, these errors appear systematic as the trends in the meteorite metal abundance data from this study align with those observed in the data from Keil (1968).
The findings of this study thus indicate that EH and EL chondrites cannot be systematically differentiated based on their metal modal abundances.

These results align with work done by Weisberg et al. (2012) that utilized an automated electron microprobe technique to assess modal abundances in unequilibrated enstatite chondrites (EH3 and EL3). Their analysis revealed that most EH3 and EL3 chondrites exhibit similar ranges in kamacite, typically ranging from 9-13 vol%, with a few EH3 chondrites showing lower kamacite abundances (4-5 vol%).

Further indicating that EH and EL chondrites cannot be systematically differentiated based on their metal content are the physical findings presented by Macke et al. (2010) on the grain densities and magnetic susceptibilities of enstatite chondrites. Their results indicate that slight differences exist between EH and EL chondrites, with EH chondrites showing slightly higher magnetic susceptibilities and grain densities. However, there is a significant degree of overlap between the two groups. The similarities observed in grain densities and magnetic

susceptibilities between EH and EL chondrites suggest that there is no significant difference in magnetic iron quantity, a finding that supports the results of this thesis.

Given the multiple studies indicating that the metal contents in EH and EL chondrites cannot be systematically distinguished, it is surprising that the assumption that EH chondrites contain more metal than EL chondrites is still so pervasive in the community, manifesting as inconsistencies in the literature.

In the classic Urey-Craig diagram [Figure 1], which plots oxidized Fe/Si on the x-axis versus reduced Fe/Si on the y-axis, EH chondrites are presented as having twice as much Fe as EL chondrites. However, the differences are not so extreme, with Fe values ranging from 22-29% in EL chondrites and 30-35% in EH chondrites (Keil, 1968). The extreme depiction in Urey-Craig diagrams is likely due to normalizing to Si. Unlike the other chondrite groups, Si does not behave as a strictly lithophile element in enstatite chondrites, being present in its reduced form in metal, schreibersite, and perryite (Keil, 1968; Baedecker & Wasson, 1975). It is suspected that such a depiction may contribute to the perpetuation of the assumption that EH chondrites have more metal than EL chondrites. However, this is just speculation.

6.1.2 Image Processing Statistical Analysis

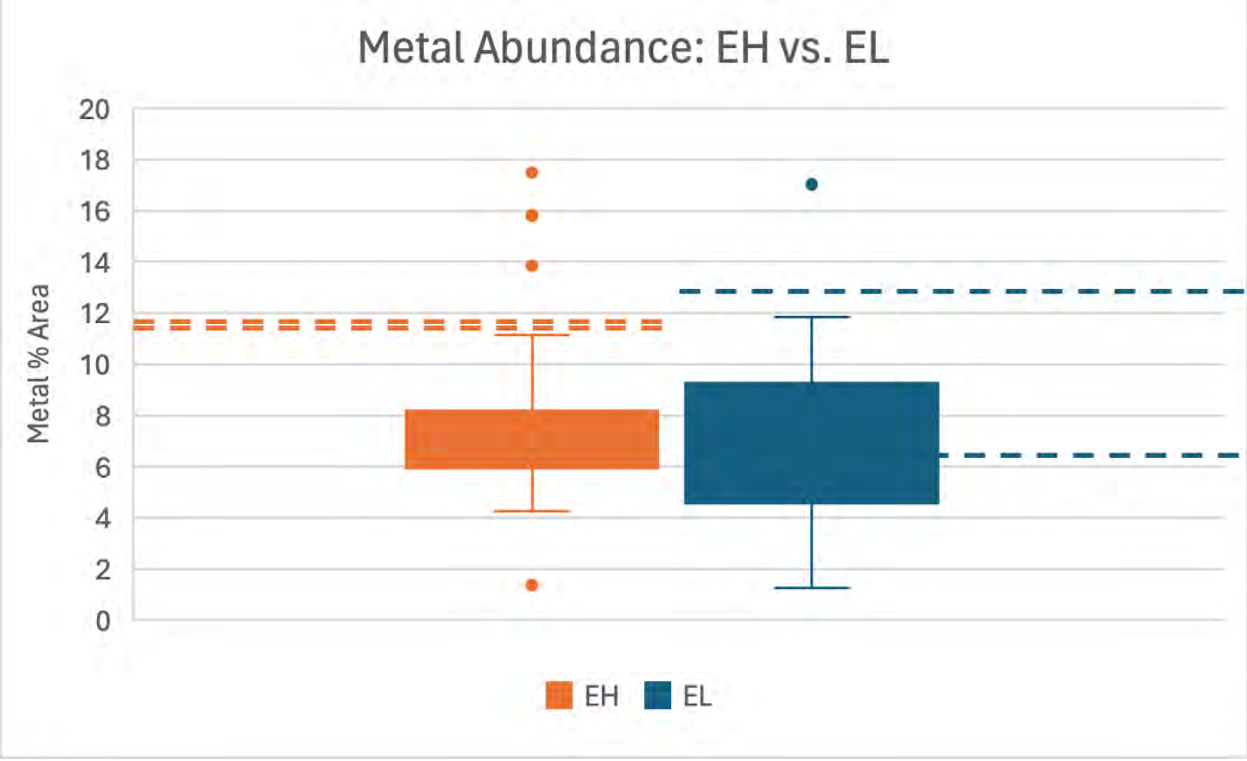

Figure 15: Box and whisker plot illustrating the spread of metal % area measurements in EH chondrites (Abee (EH4) and St. Mark's (EH5)) and EL chondrites (Daniel's Kuil (EL6) and Khairpur (EL6)). The dashed lines illustrate the data points from the Keil (1968) point counting analyses. Each dashed line corresponds to the metal modal abundance of a meteorite, converted to area % from wt. %. The data set for the EH chondrites comprises 66 data points, while the data set for the EL chondrites comprises 40 data points.

The results were subjected to a two-sample t-test assuming unequal variance to evaluate the statistical significance of metal content between EH and EL chondrites. With a significance level (α) set to 0.05, the resulting p-value was 0.088, asserting that there is no statistical difference between the amount of metal in EH versus EL chondrites. Therefore, the null hypothesis for the first stage of this study, that there is no difference in the amount of Fe-metal between EH and EL chondrites, cannot be rejected.

6.2 LA-ICP-MS

Observations made regarding metal behavior within individual meteorites are described below.

Abee (EH4):
Three metal grain analyses exhibit significant variations in their refractory highly siderophile element (HSE) patterns, whereas the remaining analyses display more uniformity [Figure 8]. This variance in behavior is intriguing and likely related to Abee's high degree of brecciation.

Indarch (EH4):
There appear to be two distinct populations of metal grains, one exhibiting lower concentrations of refractory highly siderophile elements (HSEs) than the other [Figure 8]. Upon correlating grain size measurements to the laser ablation analyses, it was observed that the population exhibiting depletions in refractory HSEs is comprised of coarse (>250 μm) metal grain analyses. Conversely, the population showing relative enrichments in refractory HSEs consists mainly of finer (60-250 μm) metal grains, with the exception of one coarse-grained analysis. Compared to the coarse-grained analyses, Cu and P concentrations are significantly more variable among the finer-grained analyses.

St. Mark's (EH5):
Concentrations between metal grains are very consistent [Figure 8]. Such consistency reveals no systematic variation in elemental abundance pattern with grain size.

Saint Sauveur (EH5):
Elemental abundance patterns between metal grains are broadly consistent, except for one analysis showing minor W and Ir depletions [Figure 8].

Daniel's Kuil (EL6):
Elemental abundance patterns are consistent across most metal grains except for one outlier, which exhibits significant depletions in Re, Os, Ir, and P and slightly elevated W and Ru concentrations [Figure 9]. There is no systematic variation in elemental abundance pattern with grain size.

Pillistfer (EL6):
Rhenium concentrations are variable between metal grains, with one analysis notably depleted in Re compared to the others [Figure 9]. Additionally, two metal grains show enrichments in W, one of which shows a remarkably high enrichment. Apart from P, which demonstrates minor variation, the other elements exhibit uniform behavior in the analyzed metal grains.

JdKL (EL6): Concentrations between metal grains are consistent, with no variation in elemental abundance pattern with grain size [Figure 9]. Minor P variations in concentrations between metal grains are present.

Khairpur (EL6):
Rhenium, Os, and W concentrations vary significantly between metal grains [Figure 9]. Additionally, Ir, Ru, and Pt concentrations vary, albeit to a lesser extent. The concentrations of the remaining elements show high consistency across the metal grains.

Observations gleaned from Figure 10 reveal several discernible trends:

1. Nickel, Co, Fe, Pd, and Au concentrations deviate minimally between samples and are the same in EH and EL chondrites to within about 4%, aligning with findings documented in the literature (Kallemeyn & Wasson, 1986).

2. The more volatile siderophile elements, namely Cu, P, Ga, and Ge, EL analyses demonstrate relatively consistent behavior compared to those of the EH chondrites.

3. Regarding the refractory siderophile elements, EH chondrites exhibit a more consistent pattern compared to the variability observed in EL chondrites. The exception is W, which sees all samples trend towards uniformity, with a relative standard deviation of 13.4%. Given that the relative standard deviations for Fe, Ni, and Co (the main constituents of kamacite) are 10.7%, 17.8%, and 9.5%, respectively, the consistency of W concentrations across samples is notable.

6.2.1 Comparison to Literature

When comparing the LA-ICP-MS data of this study with existing literature, several potential factors may contribute to the observed differences. It is plausible that the fragments analyzed in this study and those in the literature originate from different regions of the meteorites, suggesting localized chemical variations. Furthermore, it is also possible that the fragments analyzed in this study and the limited number of metal grains analyzed per sample (6-8) mean that this study's data may not be representative of the bulk sample or meteorite. Lastly, a potential source of concentration disparity between this study and the literature can be attributed to the distinct methodologies employed and the sensitivity of the instrumentation associated with each method.

Table 6: Comparison of averaged concentrations measured in metal grains in EH chondrites via LA-ICP-MS to data from the literature. | indicates conversion from wt. % to ppm.

Sample	Element	Concentration (ppm)	Concentration (ppm)
		This Work	Literature
Abee (EH4)	Ga	73	71[+]
			71[#]
	Ge	178	172[+]
			198[#]
	Au	1.99	1.35[#]
			2.13[^]
	Pd	2.97	3.71[^]
	P	3582	|5400[§]
	Fe	924986	|872000[§]
	Co	3333	|7700[§]
	Ni	71682	|82000[§]
	Cu	506	244[#]
	Ir	1.83	2.43[#]
	Os	1.75	2.95[#]
	Re	0.18	0.19[#]
			0.21[^]
	Ru	3.18	4.94[#]
	W	0.44	0.66[#]
			0.43*
Indarch (EH4)	Ga	49	61[+]
	Ge	171	192[+]
	Au	1.84	2.57[^]
	Pd	2.16	3.39[^]
	Re	0.12	0.20[^]
	P	1219	|900[§]
	Fe	797362	|893000[§]
	Co	3178	|4800[§]
	Ni	56663	|71000[§]
	W	0.42	0.46*
St. Mark's (EH5)	P	185	|500[§]
	Fe	711518	|904000[§]
	Co	2822	|4800[§]
	Ni	49750	|60000[§]
Saint Sauveur (EH5)	P	2530	|3600[§]
	Fe	970468	|895000[§]
	Co	3776	|4500[§]
	Ni	77492	|75000[§]

[+] Fouche & Smales (1967a) * Hellmann et al. (2024) [#] Rambaldi & Cendales (1980)
[^] Fouche & Smales (1967b) [§] Keil (1968)

Table 7: Comparison of averaged concentrations measured in metal grains in EL chondrites via LA-ICP-MS to data from the literature. | indicates conversion from wt. % to ppm.

Sample	Element	Concentration (ppm) This Work	Concentration (ppm) Literature
Pillistfer (EL6)	W	0.52	0.46*
	P	515	|1300§
	Fe	934404	|913000§
	Co	3690	|4900§
	Ni	61907	|63000§
Daniel's Kuil (EL6)	Ga	50	60+
	Ge	108	137+
	Au	1.84	2.35^
	Pd	2.11	3.29^
	Re	0.17	0.25^
	P	672	|1400§
	Fe	813200	|907000§
	Co	3359	|5000§
	Ni	50180	|65000§
Jaih deh Kot Lalu (EL6)	P	651	|1000§
	Fe	801057	|920000§
	Co	3300	|3700§
	Ni	48818	|62000§
Khairpur (EL6)	Ga	57	54+
			69$
	Ge	133	113+
	Cu	145	130$
	Au	1.59	1.80^
	Pd	2.36	3.50^
	Re	0.04	0.23^
	P	768	|1200§
	Fe	933905	|917000§
	Ni	62387	|69000$
			|68000§
	Co	3708	|4800§
	W	0.45	0.50*

+ Fouche & Smales (1967a) * Hellmann et al. (2024) $ Allen, R. O., Jr., & Mason, B. (1973)
^ Fouche & Smales (1967b) § Keil (1968)

The W concentrations presented in this study, measured via LA-ICP-MS, are consistent with W concentrations reported in the literature, determined through high-precision bulk sample dissolution and isotope dilution (Hellmann et al., 2024).

6.2.2 LA-ICP-MS Statistical Analysis

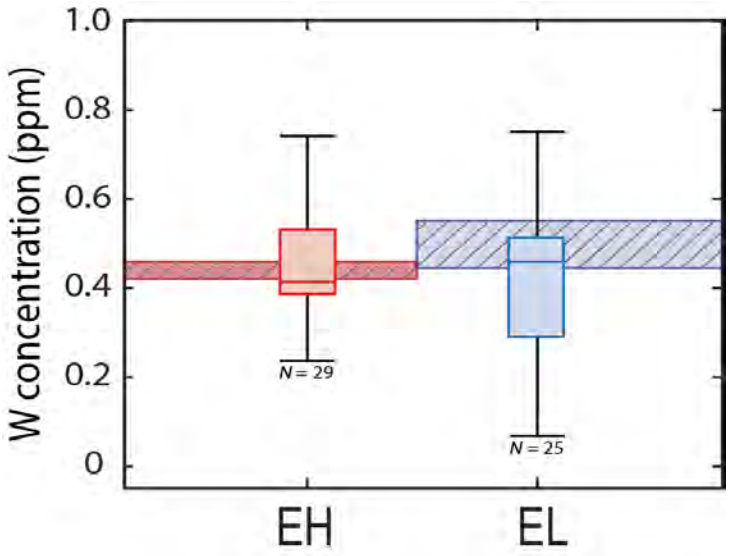

Figure 16: Box and whisker plot illustrating the spread of W concentrations in metal grains between EL and EH chondrites, compared to those determined by Hellmann et al. (2024), represented as reference bars behind the box plots. N denotes the number of samples analyzed.

A two-sample t-test assuming unequal variance was conducted to evaluate the statistical significance of W concentrations between EH and EL chondrites. With a significance level (α) set to 0.05, the resulting p-value was 0.45, affirming that there is no statistical difference between the W concentrations of EH and EL chondrites. Therefore, the null hypothesis for this portion of the study, that there is no difference in the W concentrations of the metal grains between EH and EL chondrites, is maintained.

6.3 Overall Discussion of Results

Combining the results from this study's image-processing and LA-ICP-MS portions reveals that both EH and EL chondrites have comparable metal contents with similar W concentrations, explaining the uniform W contents of bulk EH and EL chondrites. These findings support the argument that there was no physical metal silicate separation (i.e., Hf-W fractionation) between EH and EL chondrites prior to their formation.

7. Suggestions for Future Work

Using the insights gained and the limitations encountered in this work, the following section proposes several potential avenues for future research.

In this study, the sampled EH chondrites only cover petrologic types 4 and 5, and petrologic type 6 for the EL chondrites. Future work in this regard would include more samples with a wider variety of petrologic types. Such studies could contribute to our understanding of the post-accretionary histories of the enstatite chondrite parent bodies.

Furthermore, given that the samples used in this study were small fragments of larger meteorites, the analyzed fragments may not have represented the meteorite best. Therefore, in addition to expanding the sample size by including a more comprehensive petrologic range of EH and EL chondrites, repeat analyses on different fragments of the same meteorites analyzed in this study could shed light on heterogeneities within individual meteorites, informing on their accretionary and evolutionary histories. This could be looked at from a broader perspective to aid in interpretations regarding enstatite chondrite parent bodies.

Future work would benefit from machine-learning-based image segmentation, such as the Trainable Weka Segmentation Fiji plugin. In addition to improving on the metal modal abundance measurements made in this study using threshold segmentation, TWS could be used to determine modal abundances of the sulfide phase. Given the well-documented bulk-Fe measurements conducted on enstatite chondrites resolving enstatite chondrites in the high bulk-Fe EH chondrites and low bulk-Fe EL chondrites (e.g., Keil, 1968; Sears et al., 1982; Kallemeyn and Wasson, 1986), that EH and EL chondrites have the same quantity of metal necessitates that some Fe-bearing phase must be more abundant in EH chondrites than EL chondrites. As the second most prominent Fe-bearing phase in enstatite chondrites, it thus makes logical sense to explore the modal abundance of troilite (FeS) in enstatite chondrites. Keil (1968) reports modal abundances for troilite (FeS) in enstatite chondrite finds ranging from 5.8-9.8% in EH chondrites to ranging from 4.6-9.5% in EL chondrites. Evaluating sulfide content using image processing would expand the dataset, which currently consists solely of the point-counting analyses from Keil (1968). Additionally, due to their susceptibility to degradation, the sulfide grains were too texturally complex to be measured using threshold segmentation. In this respect, applying machine-learning-based image segmentation would be essential.

Lastly, this study only examined W in the metal phase. Exploring W concentrations in the silicate and sulfide phases could provide new insights into W fractionation and aid in our understanding of this element's geochemical behavior in highly reduced environments. Furthermore, evaluations of the distribution of W between the metal, sulfide, and silicate phases could contribute insight into the nature of post-accretionary processing experienced by the enstatite chondrite parent bodies.

8. Conclusions and Broader Implications

To summarize this study, enstatite chondrites are divided into high-iron EH and low-iron EL chondrites. Given the highly reduced nature of enstatite chondrites, as determined from their mineral and chemical compositions, it has been largely assumed that the majority of Fe exists in its metallic state. High-Fe EH chondrites are thus expected to contain higher quantities of metal and siderophilic W. Conversely, low-Fe EL chondrites are assumed to have less metal and correspondingly lower amounts of W. However, high-precision bulk Hf/W concentrations for enstatite chondrites show that W concentrations are nearly the same in both EH and EL chondrites. This results in a discrepancy between expected and observed W quantities. This study addressed the disparity between predicted and observed amounts of siderophilic tungsten in high-Fe EH group chondrites and low-Fe EL group chondrites by (1) quantifying the metal, sulfide and silicate content in EH and EL chondrites using image processing and (2) determining the concentration of W in the metal phase using laser ablation inductively coupled plasma mass

spectrometry (LA-ICP-MS). Results obtained from imaging analyses indicate no systematic difference between the metal content of EH and EL chondrites, with EL chondrites ranging from 1-17% metal by area, and EH chondrites ranging from 4-17% metal by area. Data collected from LA-ICP-MS analyses of metal grains reveal uniform average W concentrations between EH and EL chondrites, with values of 0.43 ppm and 0.5 ppm, respectively. These findings support the argument that there was no physical metal-silicate separation (i.e., Hf-W fractionation) between EH and EL chondrites or their precursor material. Enstatite chondrites, therefore, can be considered to provide good proxies for the compositions of meteorite parent bodies that formed in this region of the protoplanetary disk (Hellmann et al. 2024).

Acknowledgments

I want to acknowledge the American Natural History Museum and the Smithsonian Institution National Museum of Natural History for providing the samples used in this study.

I am grateful to Dr. Sarah Penniston-Dorland and Dr. Megan Newcombe for allowing me access to their laboratories and lab instruments.

To Timothy Mock and Dr. Michelle Jordan: Not all heroes wear capes; some operate mass spectrometers. Thank you for coming to my rescue not once, but twice. This project would not have been feasible without you. And to Umbra, the much-needed Carnegie canine relief: your contribution was indispensable.

To my faculty advisors, Dr. Richard Ash and Dr. Philip Piccoli, without whom this work would not have been possible: Thank you for putting up with me and all of my shortcomings, for believing in me when I did not believe in myself, and for your invaluable guidance and insight. I am privileged to have had you both as my advisors.

To my family, who have tolerated me during these last nine months: your unending love and support sustain me. I would not be where I am today without you.

To Elmer, my four-legged companion: thank you for reminding me that all it takes to find happiness is some time spent outdoors. You are my sunshine.

Lastly, to R.S.: thank you for being my confidant and my source of strength. This thesis is as much a testament to my efforts as it is to the support you have given me. Your presence in my life has enriched it beyond measure, and I look forward to the many years of friendship that lie ahead of us.

Supplementary Materials

The following file includes laser ablation analyses, grain size measurements, standard errors, photomicrographs, and image-processing thresholds. It can be accessed through the University of Maryland Geology Department's online file repository.

Bibliography

Allen, R. O., Jr., & Mason, B. (1973). Minor and trace elements in some meteoritic minerals. *Geochimica et Cosmochimica Acta*, *37*(6), 1435-1456. https://doi.org/10.1016/0016-7037(73)90081-1

Baedecker, P. A., & Wasson, J. T. (1975). Elemental fractionations among enstatite chondrites. *Geochimica et Cosmochimica Acta*, *39*(5), 735-765. https://doi.org/10.1016/0016-7037(75)90013-7

Barrat, J.-A., Bischoff, A., & Zanda, B. (2023). Trace element redistributions during metamorphism of E-chondrites: Implications for reduced bodies and the Earth. *Geochimica et Cosmochimica Acta*, *356*, 51-65. https://doi.org/10.1016/j.gca.2023.07.003

Fouche, K. F., & Smales, A. A. (1967a). The distribution of trace elements in chondritic meteorites. 1. Gallium, germanium and indium. *Chemical Geology*, *2*, 5-33. https://doi.org/10.1016/0009-2541(67)90002-2

Fouche, K. F., & Smales, A. A. (1967b). The distribution of trace elements in chondritic meteorites. 2. Antimony, arsenic, gold, palladium and rhenium. *Chemical Geology*, *2*, 105-134. https://doi.org/1016/0009-2541(67)90011-3

Hellmann, J. L., Van Orman, J. A., & Kleine, T. (2024). Hf-W isotope systematics of enstatite chondrites: Parent body chronology and origin of Hf-W fractionations among chondritic meteorites. *Earth and Planetary Science Letters*, *626*. https://doi.org/10.1016/j.epsl.2023.118518

Javoy, M., Kaminski, E., Guyot, F., Andrault, D., Sanloup, C., Moreira, M., Labrosse, S., Jambon, A., Agrinier, P., Davaille, A., & Jaupart, C. (2010). The chemical composition of the Earth: Enstatite chondrite models. *Earth and Planetary Science Letters*, *293*(3-4), 259-268. https://doi.org/10.1016/j.epsl.2010.02.033

Kallemeyn, G. W., & Wasson, J. T. (1986). Compositions of enstatite (EH3, EH4,5, and EL6) chondrites: Implications regarding their formation. *Geochimica et Cosmochimica Acta*, *50*, 2153-2164. https://doi.org/10.1016/0016-7037(86)90070-0

Keil, K. (1968). Mineralogical and Chemical Relationships among Enstatite Chondrites. *Journal of Geophysical Research*, *73*(22), 6869-7219. https://doi.org/10.1029/JB073i022p06945

Kleine, T., Touboul, M., Bourdon, B., Nimmo, F., Mezger, K., Palme, H., Jacobsen, S. B., Yin, Q.-Z., & Halliday, A. N. (2009). Hf-W chronology of the accretion and early evolution of asteroids and terrestrial planets. *Geochimica et Cosmochimica Acta*, *73*(17), 5150-5188. https://doi.org/10.1016/j.gca.2008.11.047

Kleine, T., Touboul, M., Van Orman, J. A., Bourdon, B., Maden, C., Mezger, K., & Halliday, A. N. (2008). Hf-W thermochronometry: Closure temperature and constraints on the

accretion and cooling history of the H chondrite parent body. *Earth and Planetary Science Letters*, *270*(1-2), 106-118. https://doi.org/10.1016/j.epsl.2008.03.013

Kleine, T., & Walker, R. J. (2017). Tungsten Isotopes in Planets. *Annual Review of Earth and Planetary Sciences*, *45*, 389-417. https://doi.org/10.1146/annurev-earth-063016-020037

Krot, A. N., Keil, K., Scott, E. R. D., Goodrich, C. A., & Weisberg, M. K. (2014). 1.1 Classification of Meteorites and Their Genetic Relationships. In K. K. Turekian & H. D. Holland (Eds.), *Treatise on Geochemistry* (2nd ed., pp. 1-63). https://doi.org/10.1016/B978-0-08-095975-7.00102-9

Lee, D.-C., & Halliday, A. N. (2000). Accretion of Primitive Planetesimals: Hf-W Isotopic Evidence from Enstatite Chondrites. *Science*, *288*(5471), 1629-1631. https://doi.org/10.1126/science.288.5471.1629

Lin, Y., & El Goresy, A. (2002). A comparative study of opaque phases in Qingzhen (EH3) and MacAlpine Hills 88136 (EL3): Representatives of EH and EL parents bodies. *Meteoritics and Planetary Science*, *37*(4), 577-599. https://doi.org/10.1111/j.1945-5100.2002.tb00840.x

Lodders, K., & Fegley, B. Jr. (1998). *The Planetary Scientist's Companion* (1). Oxford University Press.

Macke, R. J., Consolmagno, G. J., Britt, D. T., & Hutson, M. L. (2010). Enstatite chondrite density, magnetic susceptibility, and porosity. *Meteoritics & Planetary Science*, *45*(9), 1513-1526. https://doi.org/10.1111/j.1945-5100.2010.01129.x

Mason, B. (1966). The enstatite chondrites. *Geochimica et Cosmochimica Acta*, *30*, 23-39. https://doi.org/10.1016/0016-7037(66)90089-5

Rambaldi, E. R., & Cendales, M. (1980). Siderophile element fractionation in enstatite chondrites. *Earth and Planetary Science Letters*, *48*(2), 325-334. https://doi.org/10.1016/0012-821X(80)90196-X

Sears, D. W. G., Kallemeyn, G. W., & Wasson, J. T. (1982). The compositional classification of chondrites. II. The enstatite chondrite groups. *Geochimica et Cosmochimica Acta*, *46*, 597-608. https://doi.org/10.1016/0016-7037(82)90161-2

The Meteoritical Society. (2023, November 18). *Meteoritical Bulletin Database*. Retrieved November 26, 2023 from https://www.lpi.usra.edu/meteor/

Urey, H. C., & Craig, H. (1953). The composition of the stone meteorites and the origin of the meteorites. *Geochimica et Cosmochimica Acta*, *4*(1-2), 36-82. https://doi.org/10.1016/0016-7037(53)90064-7

Weisberg, M. K., & Kimura, M. (2012). The Unequilibrated Enstatite Chondrites. *Chemie der Erde/Geochemistry*, *72*(2), 101-115. https://doi.org/10.1016/j.chemer.2012.04.003

White, W. M. (2020). *Geochemistry* (2nd ed.). Wiley-Blackwell.

Yoshizaki, T., Ash, R. D., Lipella, M. D., Yokoyama, T., & McDonough, W. F. (2021). Variable refractory lithophile element compositions of planetary building blocks: Insights from components of enstatite chondrites. *Geochimica et Cosmochimica Acta*, *308*, 173-187. https://doi.org/10.1016/j.gca.2021.05.057

University of Maryland Honor Statement

I pledge on my honor that I have not given or received any unauthorized assistance on this assignment/examination.